Photonic quantum simulations of SSH-type topological insulators with perfect state transfer

M. Stobińska,[1] T. Sturges,[1] A. Buraczewski,[1] W. R. Clements,[2] J. J. Renema,[3] S. W. Nam,[4] T. Gerrits,[4] A. Lita,[4] P. P. Rohde,[5] W. S. Kolthammer,[2] A. Eckstein,[2] and I. A. Walmsley[2]

[1]*Institute of Theoretical Physics, University of Warsaw, ul. Pasteura 5, 02-093 Warsaw, Poland*
[2]*Clarendon Laboratory, University of Oxford, Parks Road, Oxford OX1 3PU, United Kingdom*
[3]*Complex Photonic Systems (COPS), MESA+ Institute for Nanotechnology, University of Twente, P.O. Box 217, 7500 AE Enschede, Netherlands*
[4]*National Institute of Standards and Technology, 325 Broadway, Boulder, CO 80305, USA*
[5]*Centre for Engineered Quantum Systems, Department of Physics and Astronomy, Macquarie University, Sydney NSW 2113, Australia and Centre for Quantum Computation and Intelligent Systems (QCIS), Faculty of Engineering & Information Technology, University of Technology, Sydney, NSW*

Topological insulators could profoundly impact the fields of spintronics, quantum computing and low-power electronics[1, 2]. To enable investigations of these non-trivial phases of matter beyond the reach of present-day experiments, quantum simulations provide tools to exactly engineer the model system and measure the dynamics with single site resolution[3–8]. Nonetheless, novel methods for investigating topological materials are needed, as typical approaches that assume translational invariance are irrelevant to quasi-crystals[9, 10] and more general non-crystalline structures[11]. Here we show the quantum simulation of a non-crystalline topological insulator using multi-photon interference. The system belongs to the same chiral orthogonal symmetry class as the SSH model, and is characterised by algebraically decaying edge states. In addition, our simulations reveal that the Hamiltonian describing the system facilitates perfect quantum state transfer of any arbitrary edge state. We provide a proof-of-concept experiment based on a generalised Hong–Ou–Mandel effect, where photon-number states impinge on a variable coupler.

Topological insulators are materials with an insulating bulk, and topologically protected states on their boundaries which are robust to impurities[12]. Such exotic electronic properties originate in the symmetries of physical systems and are captured by topological invariants. The simplest model presenting topological behaviour is the Su–Schrieffer–Heeger (SSH) model[13] that describes a one-dimensional dimerised chain of atoms. The particular flavour of symmetries (chiral, time-reversal and charge-conjugation symmetry) endow the topology of the system with a non-trivial character, which has the physical consequence of topologically protected zero-energy edge states. This seminal model which explained the formation of solitons in long polyacetylene chains[14] has been investigated in several physical systems[15, 16] and generalised to various models with different interactions and symmetries[17, 18]. Despite promising results [12], topological insulators have only been identified and studied in a fraction of a percent of the known crystal structures [19]. Moreover, there is a strong interest in investigating topological systems that lack translational invariance [9–11]. Thus, simulation techniques that treat topological insulators with rare symmetries are a welcome addition to the field. Whilst 2D and 3D topological insulators are renowned for their robust edge conduction channels [12], there is a growing interest in the transport of quantum states in 1D topological systems. The prediction that the state of a single qubit can be perfectly transported across a 1D chain [20] has recently been demonstrated for photons [21] and superconducting charge qubits [22]. It has been proposed to extend this process to topological systems, as they provide protection against perturbation and disorder [23].

Quantum simulations exploit well-controlled platforms to deliver new insights into complex phenomena which have so far evaded experimental realisation. They have allowed researchers to observe the dynamics of topological currents and defects in topological insulators, and directly measure their topological invariants[4–6]. A recent striking example is the simulation of the topological Anderson insulator phase[7, 8]. One frequent approach to quantum simulations is quantum walks (QWs). QWs facilitate building complex evolutions from simple steps, each performed by a local unitary. Quantum integrated optics is very well suited to this task because it permits the creation, manipulation and readout of photonic quantum states in a highly controlled manner, with high speeds and low losses [24]. Indeed, topologically protected bound states have been demonstrated with photonic QWs[25, 26].

QWs are the quantum analogy of random walks in which an initially localised particle (a walker) evolves into a superposition of many positions in space[27–29]. One important kind of QWs are continuous time QWs (CTQWs) where space is discrete and represented by a graph, and time is continuous[28]. CTQWs describe an evolution of the walker generated by a Hamiltonian H. The Hamiltonian sets the amplitudes of hopping from a graph vertex Δ_l to Δ_k per unit time, $q_{k,l} = \langle\Delta_k| H |\Delta_l\rangle$. The amplitudes are zero for disjoint vertices. The walker, initially in $|\Delta_l\rangle$, is in a superposition state $e^{-iHt}|\Delta_l\rangle$ at time t . The probability distribution of its final position $p(\Delta_k|\Delta_l)=|\langle\Delta_k| e^{-iHt} |\Delta_l\rangle|^2$

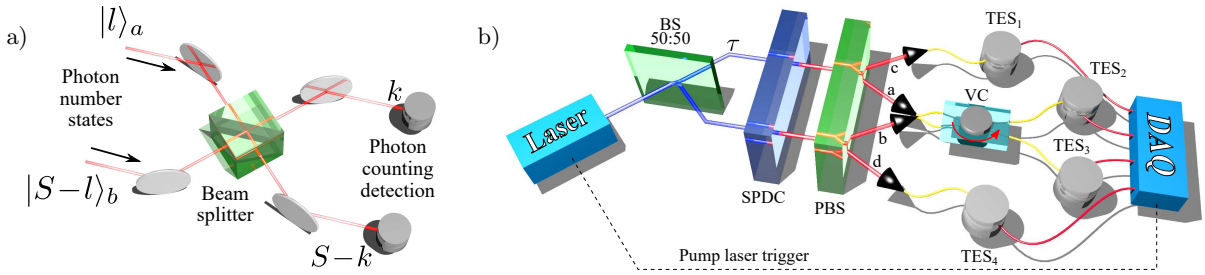

FIG. 1: **Photonic simulation of a generalised SSH topological insulator.** a) Experimental realisation is based on interference of photon-number states on a beam splitter (BS) with a variable splitting ratio, followed by photon-number-resolved detection. b) Setup: Laser – titanium-sapphire laser pump (blue), BS 50 : 50 – balanced beam splitter, τ – optical phase delay, SPDC – spontaneous parametric down conversion waveguide chip fabricated from periodically-poled potassium titanyl phosphate (PP-KTP) which produces photon-number correlated states (red), PBS – polarisation beam splitter, VC – variable coupler, TES – transition edge sensors, DAQ – data acquisition unit.

is peaked at the graph edges and has a variance which scales quadratically with time (ballistic spread). This is in contrast to a random walk where the distribution is binomial (linear spread). Most implementations of QWs that allow a single particle to take n steps, require at least $O(n)$ detectors to measure the walker's final position [30]. Thus, they are quite resource-ineffective and suffer from error accumulations that prevent the simulations of longer times.

Here we simulate a generalised SSH topological insulator which is capable of perfect quantum state transfer, by means of multi-particle bosonic quantum interference. The model belongs to the chiral orthogonal class of topological insulators [31] and reveals weakly localised edge states. This new system features similarities to the SSH topological insulator brought close to its topological phase-transition. The modification w.r.t. the original SSH model lies in fully site-dependent couplings between the chain sites which deprives the system of translational invariance. Our simulation is an analogue of a CTQW that requires only a single step to calculate the outcome of an arbitrarily long QW. It avoids error-accumulation losses which occur during numerous steps in QWs and brings the number of optical components to a minimum at the expense of increasing the number of interfering particles. It is experimentally implemented by interference of photon-number states (light pulses with a definite particle number) on a beam splitter with an adjustable splitting ratio. It relies on a multi-particle Hong–Ou–Mandel effect, which we experimentally observed for states with up to four photons. The total number of interfering particles S allows us to simulate a generalised SSH topological insulator with up to $S+1$ sites.

A pair of photon-number (Fock) states, $|l\rangle_a = \frac{(a^\dagger)^l}{\sqrt{l!}}|0\rangle$ and $|S-l\rangle_b = \frac{(b^\dagger)^{S-l}}{\sqrt{(S-l)!}}|0\rangle$, interfering on a beam splitter show a multi-photon Hong–Ou–Mandel effect, Fig. 1a. Here $a^\dagger$ and $b^\dagger$ denote photonic creation operators which act on the beam splitter input modes. For a given total number of photons S, the beam splitter input state is fully determined by the imbalance $\Delta_l^S = S-2l$ between the occupation of the input modes, which we denote as $|\Delta_l^S\rangle \equiv |l\rangle_a |S-l\rangle_b$. A beam splitter interaction between these inputs, $U_{BS}^{(r,\varphi)} = e^{-i\theta(r)H_{BS}}$, is governed by a Hamiltonian

$$H_{BS} = \tfrac{i}{2}(a^\dagger b e^{-i\varphi} - a b^\dagger e^{i\varphi}), \tag{1}$$

where $r = \sin^2\frac{\theta}{2}$ is the beam splitter reflectivity (defined as the probability of reflection of a single photon) and φ is the phase difference between the reflected and transmitted fields[32]. In the case of a balanced beam splitter ($r=0.5$), two photons arriving at the input ports will leave through the same exit port. This is known as photon bunching[33]. Similar effects hold for multi-photon-number states [34] with two equally populated modes, where the most probable event is for all photons to exit together from one port, with decreasing probabilities for less bunched states. This is reflected in the probabilities of detecting the states $|k\rangle$ and $|S-k\rangle$ behind the beam splitter, $p_S^{(r)}(k,l) = |\langle\Delta_k^S|U_{BS}^{(r,\pi/2)}|\Delta_l^S\rangle|^2 = |\phi_k^{(r)}(l-Sr,S)|^2$, where $\phi_k^{(r)}(x,y)$ denotes a Kravchuk function[35, 36]. Since$p_S^{(r)}(k,l)$ is independent of φ, for convenience we set $\varphi=\frac{\pi}{2}$ to keep the matrix representation of H_{BS} real-valued in the Fock-state basis. For more information see Supplementary Sections I and II.

Multiphoton Hong–Ou–Mandel interference allows one to complete a CTQW generated by H_{BS} in a single step. After the beam splitter, the infinitesimal evolution turns $|\Delta_l^S\rangle$ into a superposition

$$H_{BS}|\Delta_l^S\rangle = q_{l+1,l}^{(S)}|\Delta_{l+1}^S\rangle - q_{l-1,l}^{(S)}|\Delta_{l-1}^S\rangle\,. \tag{2}$$

Equation (2) provides the physical interpretation of Δ_l^S as the starting position of the walker in the graph, from where

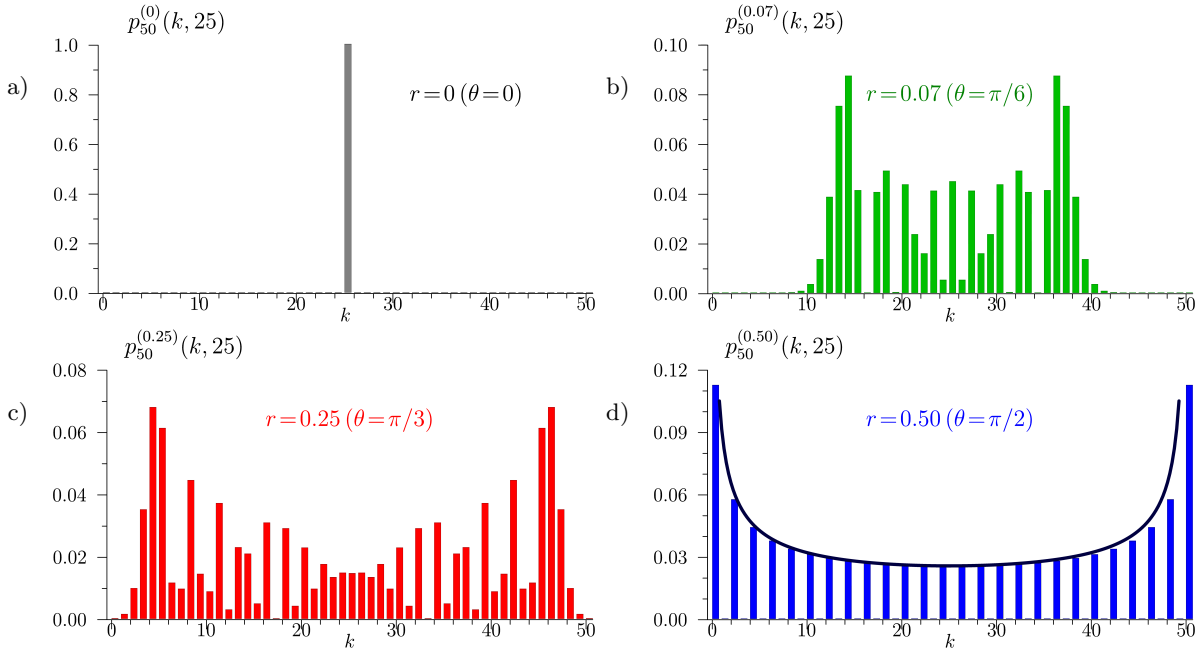

FIG. 2: **Quantum simulation implemented by multi-photon Hong–Ou–Mandel quantum interference.** Probability distributions of final positions $p_{50}^{(r)}(k,l)$ for a walker initially localised at site $l = S/2$. The beam splitter reflectivities are: a) $r = 0$, b) $r = 0.07$, c) $r = 0.25$, and d) $r = 0.50$. The reflectivities correspond to the duration of the quantum walk θ. The black curve represents the envelope of a weakly localised edge state.

it moves to the right $|\Delta_{l+1}^S\rangle$ or left $|\Delta_{l-1}^S\rangle$ with jump probability amplitudes

$$q_{l+1,l}^{(S)} = q_{l,l+1}^{(S)} = \tfrac{1}{2}\sqrt{(S+\Delta_l^S)(S-\Delta_l^S+2)}. \tag{3}$$

The total number of particles S confines the region of evolution to $S+1$ points, from $\Delta_S^S = -S$ to $\Delta_0^S = S$. Distribution of the walker's final position is given by $p(\Delta_k^S|\Delta_l^S) = p_S^{(r)}(k,l)$, where the beam splitter reflectivity r controls the evolution time of the quantum walk which is simulated. The spectrum of H_{BS} is harmonic and the evolution is periodic, and thus we need only consider values $0 \le \theta \le 1$, for which $r \approx \theta^2/4$. The variance reveals a ballistic spread, which with this approximation reads

$$\mathrm{Var}(\Delta_k^S) = \frac{\theta^2(r)}{4}\left(\frac{S^2-(\Delta_l^S)^2}{2}+S\right), \tag{4}$$

(see Supplementary Section III for derivation). Sample distributions are depicted in Fig. 2.

Decoherence deforms the QW statistics towards the binomial distribution [37]. This effect is also present in our simulation where the degree of coherence can be controlled by the distinguishability of particles (see Supplementary Section IV). If one of the beams comes in a superposition of two orthogonal polarisations $b^\dagger \to \cos y\, b^\dagger + \sin y\, b_\perp^\dagger$, whereas the other beam is in a single polarisation $a^\dagger \to a^\dagger$, then $0 \le y \le \frac{\pi}{2}$ 'tunes' the distinguishability between the modes. For $y = 0$ they are indistinguishable, while $y = \frac{\pi}{2}$ makes $|l\rangle$ and $|S-l\rangle$ orthogonally polarised. Since a beam splitter sees orthogonal modes independently, the model can be extended to higher dimensions, for example by including spectral degrees of freedom.

We now show how Fock state interference on a beam splitter facilitates the quantum simulation of a generalised SSH model. First, consider a general chiral XY spin-chain represented by the Hamiltonian

$$H_{XY} = \sum_{n=1}^{S} \tfrac{J_n}{2}\left(\sigma_n^x\sigma_{n+1}^x + \sigma_n^y\sigma_{n+1}^y\right), \tag{5}$$

where σ_n^x and σ_n^y are the Pauli operators acting on the nth spin. When restricted to the single excitation subspace spanned by the states $|n\rangle = \sigma_n^+ |\downarrow\downarrow\downarrow\ldots\rangle$ where $\sigma_n^\pm = (1/2)\left(\sigma_n^x \pm i\sigma_n^y\right)$ is the raising operator, this model has matrix

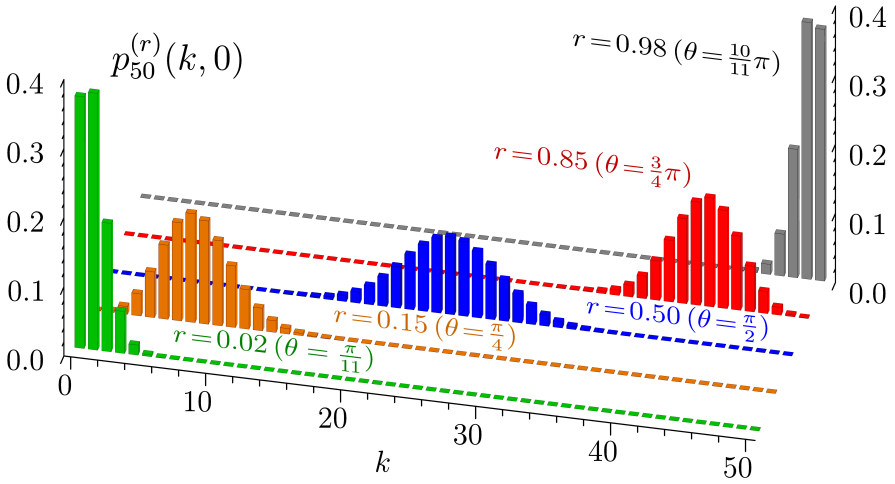

FIG. 3: **Perfect state transfer implemented by multi-photon Hong–Ou–Mandel quantum interference.** For an input corresponding to an edge state localised on the left of the chain, the beam splitter interaction simulates the perfect state transfer of this edge state to the other side.

elements $[\mathbf{H}_{XY}]^{\text{Spin}}_{mn} = \langle m| H_{XY} |n\rangle = J_n\delta_{n,m+1} + J_m\delta_{m,n+1}$. Couplings of the form $J_n = 2J(1+\delta(-1)^n)$ would correspond to the original SSH model, where δ governs the dimerisation. For $\delta > 0$ it reveals topologically-protected edge states, e.g. near the left end of the chain of the form $\sum_{n=1}^{(S+1)/2}(-1)^n e^{-2n/\xi}\sigma^+_{2n}|{\downarrow\downarrow\downarrow}\ldots\rangle$, where ξ is the localisation length[38].

Now consider the matrix elements of the photonic Hamiltonian in the Fock state basis, $[\mathbf{H}_{\text{BS}}]^{\text{Fock}}_{nm} = \langle\Delta^S_n| H_{\text{BS}} |\Delta^S_m\rangle$. We find that the photonic and XY matrix representations are identical $[\mathbf{H}_{\text{BS}}]^{\text{Fock}}_{nm} = [\mathbf{H}_{XY}]^{\text{Spin}}_{nm}$ when we set the spin-couplings to $J_n = (1/2)\sqrt{n(S+1-n)}$[20]. In this case the system completely lacks translational invariance, but also belongs to the chiral orthogonal (BDI) class of Altland–Zirnbauer symmetry classes which are characterised by a $\mathbb{Z}$ topological invariant (see Supplementary Section V). Thus, rather remarkably, we see that two-mode Fock state interference is capable of simulating a non-crystalline topological material. Its zero-energy eigenmode is of the form $\sum_{k=0}^{S} e^{-i\frac{\pi}{2}(S/2-k)}\,\phi_k^{(1/2)}(0,S)\,\sigma^+_{k+1}|{\downarrow\downarrow\downarrow}\ldots\rangle$ (see Supplementary Section VI for derivation). This weakly localised edge state features an algebraically decaying envelope given by $\frac{4}{\pi S\sqrt{1-(2k/S-1)^2}}$, Fig. 2(d). We note that the original SSH model can also present weakly localised edge states with a numerically comparable envelope, when brought close to its topological transition (see Supplementary Section V).

Moreover, we discover that the Hamiltonian in Eq. (5) facilitates perfect quantum state transfer [20] of any arbitrary edge state over a finite chain. To demonstrate this behaviour we performed an experimental simulation of the state transfer of an SSH-like strongly localised edge state. Such a quantum simulation has been visualised in Fig. 3, where the initial Fock state $|0,S\rangle$ gradually transforms into $|S,0\rangle$ for r (which plays the role of time) changing from 0 to 1. Mathematically, the beam splitter interaction performs an α-fractional Quantum Kravchuk-Fourier transform (α-QKT) of the input state with fractionality $\alpha = 4\arcsin\sqrt{r}/\pi$ [35]. The 2-QKT is the spatial inversion operator [36] (mirror reflection), and thus impinging any edge state onto a beam splitter with reflectivity $r = 1$ corresponds to a perfect state transfer of that state to the other end of the chain.

Fig. 1b shows the experimental schema used for quantum simulations by means of the multi-photon Hong–Ou–Mandel effect. Two pulsed spontaneous parametric down-conversion (SPDC) sources each generate two-mode photon-number correlated states (see Supplementary Section VII). The modes are separated with a polarizing beam splitter into the spatial modes a–d. The idler beams c and d are used for heralding the creation of the signal Fock states $|l\rangle$ in a and $|S-l\rangle$ in b which interfere in a variable ratio fibre coupler (the beam splitter). Photon-number statistics are measured with photon-number-resolved detection implemented by transition edge sensors with efficiency exceeding 90%[39]. The optimal temporal overlap at the beam splitter was achieved by adjusting an optical path delay τ.

For a small parametric gain, the probability of creating a pair of n-photon states is approximately $\lambda_n = \langle n\rangle^n$. The average photon number was $\langle n\rangle \approx 0.2$, which provided sufficient multi-photon events. For example, as the repetition rate of the pump was 75 kHz, approximately 12 four-photon Fock states were generated per minute in each arm of the SPDC, of which about 6 reached the detectors due to $\sim 50\%$ losses in the setup. There was no post-selection, rather we recorded those events which were multi-photon, as heralded by the idler beam.

We interfered a multi-photon Fock state $|\Delta^4_2\rangle$ on a coupler with splitting ratios $r = 0.04$ (green), 0.3 (red), 0.5 (blue)

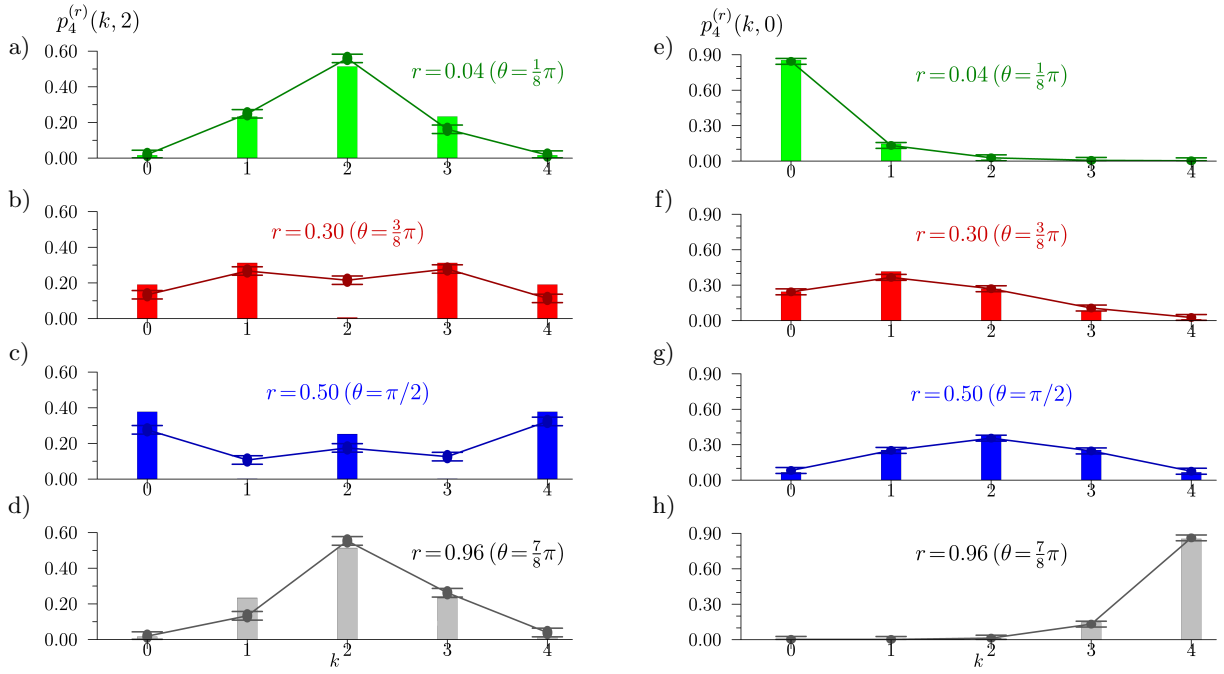

FIG. 4: **Photon number statistics resulting from Fock state $|l, S-l\rangle$ interference.** The probabilities of detecting $|k\rangle$ and $|S-k\rangle$ photons behind the beam splitter for input a–d) $|2,2\rangle$ and e–h) $|0,4\rangle$. The beam splitter reflectivities are a) & d) $r=0.04$ (green), b) & e) 0.3 (red), c) & f) 0.5 (blue) and d) & h) 0.96 (grey). Vertical bars represent theoretical values for an ideal system, while dots with error bars are values determined in experiment.

and $r=0.96$ (grey), and measured photon-number statistics, Fig. 4a–d. They correspond to CTQWs generated by $H_{\rm BS}$ for $\theta=0.40$, 1.16, 1.57 and 2.74, respectively. Variances of the distributions are $\mathrm{Var}(\Delta_k^S)=0.49$, 4.03, 7.40 and 0.49, which is in agreement with Eq. (4) and proves the ballistic spread. The result obtained for $r=0.5$ (blue) shows a zero-energy eigenmode of a generalised SSH model described by $[\mathbf{H}_{\rm BS}]^{\rm Fock}_{nm}$, which reveals two weakly localised edge states with an algebraically decaying envelope. Errors were estimated as a square root inverse of the number of measurements.

Next, the vacuum $|0\rangle$ was impinged with multi-photon Fock states $|4\rangle$ (giving an input state of $|\Delta_0^4\rangle$) at the beam splitter with splitting ratios $r=0.04$ (green), 0.3 (red), 0.5 (blue) and 0.96 (grey), Fig. 4e–h. This process simulates perfect state transfer of the first spin in the chain of 5 particles for subsequent time instances $\theta=0.40$, 1.16, 1.57, and 2.74, respectively.

In conclusion, we have demonstrated that the quantum interference of multi-photon Fock states on a beam splitter is capable of simulating a non-crystalline topological material. The Hamiltonian of our simulation corresponds to a Kravchuk transform [35] that is computationally expensive to perform classically. Whereas in the quantum domain this simulation has a computational complexity of just $O(1)$, which gives a clear quantum advantage. The system is characterised by a lack of translational invariance, and also belongs to the same chiral orthogonal symmetry class of 1D systems as the SSH model [40]. Examples of such materials include superconducting nanowires[40, 41], disordered graphene quasi-1D nanoribbons[42], disordered cold atoms[43] and quasi-1D organic superconductors[44]. These may find applications in next generation electronics[45] and spintronics[46] operating with almost no energy dissipation and offering speeds exceeding 100 GHz. In addition, our system is capable of the perfect quantum state transfer of an arbitrary quantum state, which is a requirement for information interchange in quantum computers operating on localised qubits[23, 47]. We showed this experimentally for a state initially localized on one site. From the point of view of fundamental research a beam splitter implements an exchange interaction, one of the most ubiquitous interactions in condensed matter systems. Thus, our simulations could be further used to model, for example, exciton-polariton superfluids [48] with sub-Poissonian statistics, which is also beyond the capabilities of current technology.

Acknowledgments

Acknowledgements MS, TS and AB were supported by the Foundation for Polish Science "First Team" project No. POIR.04.04.00-00-220E/16-00 (originally: FIRST TEAM/2016-2/17). AE and IW were supported by the Engineering and Physical Sciences Research Council project No. EP/K034480/1. MS thanks Paweł Kurzynski for discussions on quantum walks.

Contributions MS, TS, AB and PPR developed the theory while AE, WRC, WSK, and IAW were responsible for realization of the experiment. JJR, SWN, TG, and AL delivered and maintained the transition edge sensor detection system. AB and AE developed the software and performed numerical computations. AB prepared the plots. All the co-authors wrote up the manuscript.

Competing Interests The authors declare that they have no competing financial interests.

Correspondence All data needed to evaluate the conclusions in the paper are present in the paper and/or the Supplementary Information. Additional data available from authors upon request.

---

[1] N. H. D. Khang, Y. Ueda, and P. N. Hai, Nat. Mater. **17**, 808 (2018).

[2] C. Nayak, S. H. Simon, A. Stern, M. Freedman, and S. Das Sarma, Rev. Mod. Phys **80**, 1083 (2008), URL https://link.aps.org/doi/10.1103/RevModPhys.80.1083.

[3] I. M. Georgescu, S. Ashhab, and F. Nori, Rev. Mod. Phys **86**, 153 (2014), URL https://link.aps.org/doi/10.1103/RevModPhys.86.153.

[4] N. Goldman, J. C. Budich, and P. Zoller, Nat. Phys. **12**, 639 (2016).

[5] A. D. King, J. Carrasquilla, J. Raymond, I. Ozfidan, E. Andriyash, A. Berkley, M. Reis, T. Lanting, R. Harris, F. Altomare, et al., Nature **560**, 456 (2018).

[6] L. Lu, J. D. Joannopoulos, and M. Soljačić, Nat. Photonics **8**, 821 (2014).

[7] E. J. Meier, F. A. An, A. Dauphin, M. Maffei, P. Massignan, T. L. Hughes, and B. Gadway, Science **11**, 1 (2018), URL https://science.sciencemag.org/content/early/2018/10/10/science.aat3406.

[8] S. Stützer, Y. Plotnik, Y. Lumer, P. Titum, N. H. Lindner, M. Segev, M. C. Rechtsman, and A. Szameit, Nature **560**, 461 (2018).

[9] Y. E. Kraus, Y. Lahini, Z. Ringel, M. Verbin, and O. Zilberberg, Phys. Rev. Lett. **109**, 106402 (2012), URL https://link.aps.org/doi/10.1103/PhysRevLett.109.106402.

[10] M. A. Bandres, M. C. Rechtsman, and M. Segev, Phys. Rev. X **6**, 011016 (2016), URL https://link.aps.org/doi/10.1103/PhysRevX.6.011016.

[11] A. Agarwala and V. B. Shenoy, Phys. Rev. Lett. **118**, 236402 (2017), URL https://link.aps.org/doi/10.1103/PhysRevLett.118.236402.

[12] M. Z. Hasan and C. L. Kane, Rev. Mod. Phys **82**, 3045 (2010), URL https://link.aps.org/doi/10.1103/RevModPhys.82.3045.

[13] W. P. Su, J. R. Schrieffer, and A. J. Heeger, Phys. Rev. Lett. **42**, 1698 (1979), URL https://link.aps.org/doi/10.1103/PhysRevLett.42.1698.

[14] A. J. Heeger, S. Kivelson, J. R. Schrieffer, and W. P. Su, Rev. Mod. Phys **60**, 781 (1988), URL https://link.aps.org/doi/10.1103/RevModPhys.60.781.

[15] M. Atala, M. Aidelsburger, J. T. Barreiro, D. Abanin, T. Kitagawa, E. Demler, and I. Bloch, Nat. Phys. **9**, 795 (2013).

[16] C. A. Downing and G. Weick, Phys. Rev. B **95**, 125426 (2017), URL https://link.aps.org/doi/10.1103/PhysRevB.95.125426.

[17] L. Li, Z. Xu, and S. Chen, Phys. Rev. B **89**, 085111 (2014), URL https://link.aps.org/doi/10.1103/PhysRevB.89.085111.

[18] M. Maffei, A. Dauphin, F. Cardano, M. Lewenstein, and P. Massignan, New J. Phys. **20**, 013023 (2018), URL http://stacks.iop.org/1367-2630/20/i=1/a=013023.

[19] B. Bradlyn, L. Elcoro, J. Cano, M. G. Vergniory, Z. Wang, C. Felser, M. I. Aroyo, and B. A. Bernevig, Nature **547**, 298 (2017).

[20] M. Christandl, N. Datta, A. Ekert, and A. J. Landahl, Phys. Rev. Lett. **92**, 187902 (2004), URL https://link.aps.org/doi/10.1103/PhysRevLett.92.187902.

[21] R. J. Chapman, M. Santandrea, Z. Huang, G. Corrielli, A. Crespi, M.-H. Yung, R. Osellame, and A. Peruzzo, Nat. Commun. **7**, 11339 (2016).

[22] X. Li, Y. Ma, J. Han, T. Chen, Y. Xu, W. Cai, H. Wang, Y. Song, Z.-Y. Xue, Z.-q. Yin, et al., Phys. Rev. Appl. **10**, 054009 (2018), URL https://link.aps.org/doi/10.1103/PhysRevApplied.10.054009.

[23] F. Mei, G. Chen, L. Tian, S.-L. Zhu, and S. Jia, Phys. Rev. A **98**, 012331 (2018), URL https://link.aps.org/doi/10.1103/PhysRevA.98.012331.

[24] S. Tanzilli, A. Martin, F. Kaiser, M. De Micheli, O. Alibart, and D. Ostrowsky, Laser Photonics Rev. **6**, 115 (2012), URL https://onlinelibrary.wiley.com/doi/abs/10.1002/lpor.201100010.

[25] T. Kitagawa, M. S. Rudner, E. Berg, and E. Demler, Phys. Rev. A **82**, 033429 (2010), URL https://link.aps.org/doi/10.1103/PhysRevA.82.033429.

[26] T. Kitagawa, M. A. Broome, A. Fedrizzi, M. S. Rudner, E. Berg, I. Kassal, A. Aspuru-Guzik, E. Demler, and A. G. White, Nat. Commun. **3**, 882 (2012).

[27] Y. Aharonov, L. Davidovich, and N. Zagury, Phys. Rev. A **48**, 1687 (1993), URL https://link.aps.org/doi/10.1103/PhysRevA.48.1687.

[28] E. Farhi and S. Gutmann, Phys. Rev. A **58**, 915 (1998), URL https://link.aps.org/doi/10.1103/PhysRevA.58.915.

[29] J. Kempe, Contemp. Phys **44**, 307 (2003), URL https://doi.org/10.1080/0010715031000110776.

[30] L. Sansoni, F. Sciarrino, G. Vallone, P. Mataloni, A. Crespi, R. Ramponi, and R. Osellame, Phys. Rev. Lett. **108**, 010502 (2012), URL https://link.aps.org/doi/10.1103/PhysRevLett.108.010502.

[31] A. Kitaev, AIP Conf. Proc. **1134**, 22 (2009), URL https://aip.scitation.org/doi/abs/10.1063/1.3149495.

[32] M. S. Kim, W. Son, V. Bužek, and P. L. Knight, Phys. Rev. A **65**, 032323 (2002), URL https://link.aps.org/doi/10.1103/PhysRevA.65.032323.

[33] C. K. Hong, Z. Y. Ou, and L. Mandel, Phys. Rev. Lett. **59**, 2044 (1987), URL https://link.aps.org/doi/10.1103/PhysRevLett.59.2044.

[34] R. A. Campos, B. E. A. Saleh, and M. C. Teich, Phys. Rev. A **40**, 1371 (1989), URL https://link.aps.org/doi/10.1103/PhysRevA.40.1371.

[35] M. Stobińska, A. Buraczewski, M. Moore, W. R. Clements, J. J. Renema, S. W. Nam, T. Gerrits, A. Lita, W. S. Kolthammer, A. Eckstein, et al., *Quantum interference enables constant-time quantum information processing* (2018), 1807.03960.

[36] N. M. Atakishiyev and K. B. Wolf, J. Opt. Soc. Am. A **14**, 1467 (1997), URL http://josaa.osa.org/abstract.cfm?URI=josaa-14-7-1467.

[37] V. Kendon, Math. Structures Comput. Sci. **17**, 1169 (2007).

[38] P. Nevado, S. Fernández-Lorenzo, and D. Porras, Phys. Rev. Lett. **119**, 210401 (2017), URL https://link.aps.org/doi/10.1103/PhysRevLett.119.210401.

[39] P. C. Humphreys, B. J. Metcalf, T. Gerrits, T. Hiemstra, A. E. Lita, J. Nunn, S. W. Nam, A. Datta, W. S. Kolthammer, and I. A. Walmsley, New J. Phys. **17**, 103044 (2015), URL http://stacks.iop.org/1367-2630/17/i=10/a=103044.

[40] E. Dumitrescu, B. Roberts, S. Tewari, J. D. Sau, and S. D. Sarma, Phys. Rev. B **91**, 094505 (2015).

[41] M. Diez, J. P. Dahlhaus, M. Wimmer, and C. W. J. Beenakker, Phys. Rev. B **86**, 094501 (2012).

[42] M. Y. Han, B. Özyilmaz, Y. Zhang, and P. Kim, Phys. Rev. Lett. **98**, 206805 (2007).

[43] F. Pinheiro and J. Larson, Phys. Rev. A **92**, 023612 (2015).

[44] E. Dumitrescu and S. Tewari, Phys. Rev. B **88**, 220505 (2013).

[45] A. N. McCaughan and K. K. Berggren, Nano Lett. **14**, 5748 (2014).

[46] T. Nautiyal, T. H. Rho, and K. S. Kim, Phys. Rev. B **69**, 193404 (2004).

[47] L. Banchi, G. Coutinho, C. Godsil, and S. Severini, J. Math. Phys. **58**, 032202 (2017), URL https://aip.scitation.org/doi/10.1063/1.4978327.

[48] A. V. Kavokin, J. J. Baumberg, G. Malpuech, and F. P. Laussy, *Microcavities (2nd Edition)* (Oxford University Press, 2017).

[49] A. Eckstein, A. Christ, P. J. Mosley, and C. Silberhorn, Phys. Rev. Lett. **106**, 013603 (2011).

[50] T. Gerrits, N. Thomas-Peter, J. C. Gates, A. E. Lita, B. J. Metcalf, B. Calkins, N. A. Tomlin, A. E. Fox, A. L. Linares, J. B. Spring, et al., Phys. Rev. A **84**, 060301 (2011).

Supplementary information: Photonic quantum simulations of SSH-type topological insulators with perfect state transfer

I. MULTIPHOTON QUANTUM INTERFERENCE

We examine photon-number statistics behind the beam splitter with reflectivity r, see Fig.1. The probability amplitude of detecting k and $S-k$ photons provided that l and $S-l$ were injected is as follows

$$\mathcal{A}_S^{(r,\varphi)}(k,l) = \langle \Delta_k^S | \, U_{BS}^{(r,\varphi)} \, | \Delta_l^S \rangle = \langle k, S-k | \, U_{BS}^{(r,\varphi)} \, | l, S-l \rangle = e^{-i\theta\frac{S}{2}} \, e^{i\varphi(l-k)} \, (-1)^{k+l} \, \phi_k^{(r)}(l-Sr,S). \tag{S1}$$

Here $\phi_k^{(r)}(l-Sr,S)$ are orthonormal Kravchuk functions, see section II for details. Thus, photon-number statistics reads as follows

$$p_S^{(r)}(k,l) = |\mathcal{A}_S^{(r,\varphi)}(k,l)|^2 = |\phi_k^{(r)}(l-Sr,S)|^2. \tag{S2}$$

Please note that while $p_S^{(r)}(k,l)$ is governed by the reflectivity r, it is independent of the phase φ.

The output state which exits the beam splitter takes the form

$$\left| \Psi_l^{(S,r,\varphi)} \right\rangle = U_{BS}^{(r,\varphi)} \, | \Delta_l^S \rangle = U_{BS}^{(r,\varphi)} \, | l, S-l \rangle = \sum_{k=0}^{S} \mathcal{A}_S^{(r,\varphi)}(k,l) \, | k, S-k \rangle \, . \tag{S3}$$

II. KRAVCHUK FUNCTIONS

Kravchuk functions are a set of orthonormal discrete polynomials [36]

$$\sum_{l=0}^{S} \phi_n^{(r)}(l-Sr,S) \, \phi_m^{(r)}(l-Sr,S) = \delta_{n,m}. \tag{S4}$$

For large S they limit to Hermite–Gauss polynomials. They may be expressed by means of the Gauss hypergeometric function as

$$\phi_k^{(r)}(l-Sr,S) = (-1)^k \sqrt{\binom{S}{l}\binom{S}{k}} \sqrt{(1-r)^{S-l-k} \, r^{l+k}} \, {}_2F_1\left[-k,-l;-S;\tfrac{1}{r}\right]. \tag{S5}$$

Thus, we obtain an alternative expression for the photon-number statistics

$$p_S^{(r)}(k,l) = \binom{S}{l}\binom{S}{k} (1-r)^{S-l-k} \, r^{l+k} \left| {}_2F_1\left[-k,-l;-S;\tfrac{1}{r}\right] \right|^2. \tag{S6}$$

III. BALLISTIC SPREAD OF QUANTUM WALK VARIANCE

We now show that the spread of the variance of a walker's final position in the Hong-Ou-Mandel CTQW is ballistic. To do so, we will perform a mapping from the beam-splitter Hamiltonian to the Schwinger representation of the su(2) algebra. It allows one to associate two quantum-harmonic oscillator modes with spin operators as follows

$$S_x = \frac{a^\dagger b + a\, b^\dagger}{2}, \qquad S_y = \frac{i\left(a\, b^\dagger - a^\dagger b\right)}{2}, \qquad S_z = \frac{a^\dagger a - b^\dagger b}{2}, \qquad S_0 = \frac{a^\dagger a + b^\dagger b}{2}, \tag{S7}$$

where S_0 is the Casimir operator $S_0(S_0+1) = S_x^2 + S_y^2 + S_z^2$ and the standard su(2) commutation relations hold

$$[S_x, S_y] = iS_z, \qquad [S_y, S_z] = iS_x, \qquad [S_z, S_x] = iS_y. \tag{S8}$$

By using Eq. (S7) one can show that a two-mode Fock state $|\Delta_l^S\rangle = |l\rangle_a \, |S-l\rangle_b$ corresponds to an $S_z = \frac{S}{2} - l$ Dicke state, and also that

$$H_{BS} = -\left(\cos\varphi \cdot S_y - \sin\varphi \cdot S_x\right). \tag{S9}$$

For $\varphi = \frac{\pi}{2}$ then

$$H_{BS} = S_x. \tag{S10}$$

It is therefore straightforward to show that in the Heisenberg picture S_z evolves as

$$S_z(\theta) = S_z \cos\theta + S_y \sin\theta. \tag{S11}$$

Note that S_y is a linear combination of raising $S_+ = a^\dagger b$ and lowering $S_- = b^\dagger a$ operators, $S_y = \frac{i(S_- - S_+)}{2}$, therefore for the states $|\Delta_l^S\rangle$ the average value of S_y is zero and we obtain

$$\langle S_z(\theta)\rangle = \langle S_z\rangle \cos\theta. \tag{S12}$$

Moreover,

$$S_z^2(\theta) = S_z^2 \cos^2\theta + S_y^2 \sin^2\theta + \{S_y, S_z\} \cos\theta \sin\theta. \tag{S13}$$

Due to the same reason as above, for the states $|\Delta_l^S\rangle$ the average value of $S_z^2(\theta)$ equals

$$\langle S_z^2(\theta)\rangle = \langle S_z^2\rangle \cos^2\theta + \langle S_y^2\rangle \sin^2\theta. \tag{S14}$$

In addition, since $|\Delta_l^S\rangle$ are eigenstates of S_z, we have $\langle S_z^2\rangle = \langle S_z\rangle^2$. The value $\langle S_y^2\rangle$ can be evaluated in the following way. At first, we note that

$$S_y^2 = \frac{-(S_- - S_+)^2}{4} = \frac{-S_-^2 - S_+^2 + S_+S_- + S_-S_+}{4}. \tag{S15}$$

For the states $|\Delta_l^S\rangle$ we have

$$\langle S_y^2\rangle = \frac{\langle S_+S_-\rangle + \langle S_-S_+\rangle}{4} = \frac{\frac{S}{2}(\frac{S}{2}+1) - \left(\frac{\Delta_l^S}{2}\right)^2}{2}. \tag{S16}$$

Therefore

$$\mathrm{Var}[S_z(\theta)] = \langle S_z^2(\theta)\rangle - \langle S_z(\theta)\rangle^2 = \tfrac{1}{4}\left(\tfrac{S^2 - \left(\Delta_l^S\right)^2}{2} + S\right)\sin^2\theta. \tag{S17}$$

By approximating $\sin\theta \approx \theta$ we get

$$\mathrm{Var}[S_z(\theta)] \approx \tfrac{1}{4}\left(\tfrac{S^2 - \left(\Delta_l^S\right)^2}{2} + S\right)\theta^2, \tag{S18}$$

which confirms ballistic spreading. In the main text we denote $\mathrm{Var}[S_z(\theta)]$ by $\mathrm{Var}(\Delta_k^S)$. Fig. S1 shows the variance of the probability distributions of final positions of a walker as a function of the time of the walk, for various values of S and Δ_l^S.

IV. DISTINGUISHABILITY AS A FORM OF DECOHERENCE

In the presence of decoherence, QW statistics turn into the binomial distribution [37], characteristic of a random walk. We expect this effect also for the Hong–Ou–Mandel CTQW, where the degree of coherence is controlled by the distinguishability of interfering particles. Consider one beam in a particular polarisation $a^\dagger$, and the other beam in a superposition of the same polarisation $b^\dagger$ and an orthogonal one $b_\perp^\dagger$

$$b^\dagger \to \cos y\, b^\dagger + \sin y\, b_\perp^\dagger. \tag{S19}$$

The parameter $y \in (0, \frac{\pi}{2})$ introduces weights between the modes, and 'tunes' the distinguishability. The particles are fully indistinguishable if $y=0$, whereas if $y=\frac{\pi}{2}$ they are maximally distinguishable: $|l\rangle$ and $|S-l\rangle$ are orthogonally polarized. Transformation (S19) leads to the interference of $|l\rangle$ with a two-mode Fock-state superposition

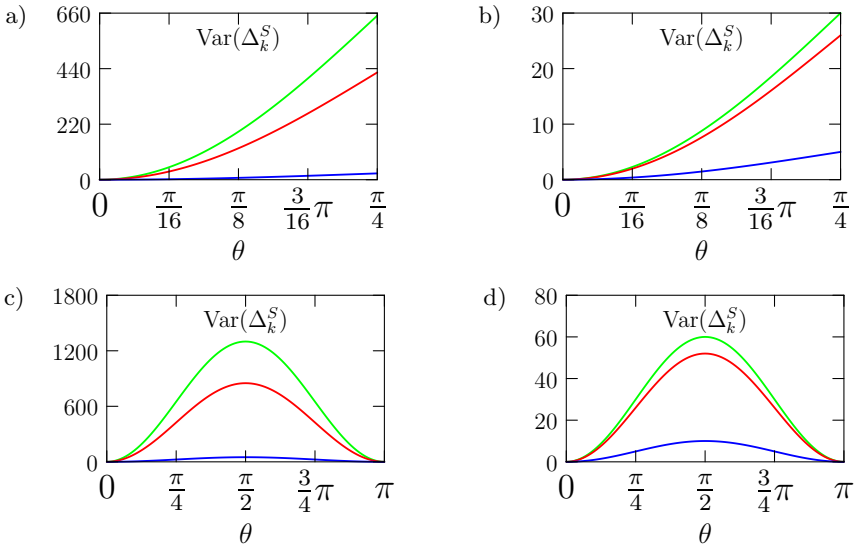

FIG. S1: Variance of the probability distributions of final positions of a walker in the Hong–Ou–Mandel CTQW as a function of walk time θ for (a) & (c) $S = 50$ and the initial position of the walker $\Delta_l^S = 0$ (green), $\Delta_l^S = 30$ (red) and $\Delta_l^S = 50$ (blue); (b) & (d) $S = 10$ and $\Delta_l^S = 0$ (green), $\Delta_l^S = 4$ (red) and $\Delta_l^S = 10$ (blue).

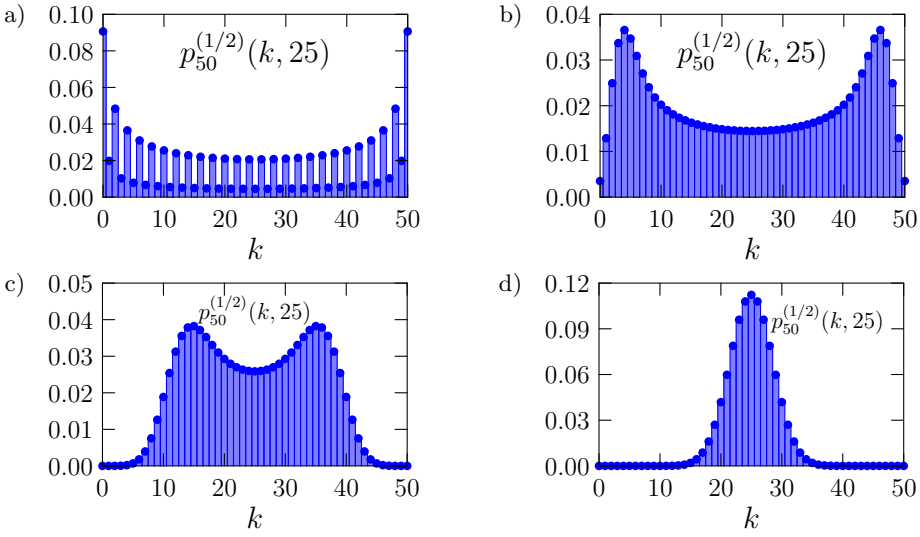

FIG. S2: Modification of the probability distribution depicted in Fig. 2(d) of the main text in blue ($l = 25$, $r = \frac{1}{2}$), for various degrees of distinguishability of particles: (a) $y = \pi/24$, (b) $y = \pi/6$, (c) $y = \pi/3$ and (d) $y = \pi/2$ (fully distinguishable).

$\sum_{n=0}^{S-l} \binom{S-l}{n}^{-1/2} \cos^n y \, (\sin y)^{S-l-n} \, |n\rangle \, |S-l-n\rangle_\perp$, instead of the single-mode Fock state $|S-l\rangle$, as before.

In Fig. S2 we show how the doubly-peaked distribution from Fig. 2 of the main text changes if the particles become distinguishable. With increasing y, full cancellation of certain events is impossible and the two peaks gradually shift to the centre of the line and merge to create the binomial distribution for $y = \frac{\pi}{2}$. Distinguishability mimics decoherence because it leads to interference of the multi-photon states with the vacuum state thus, it implements the usual model describing particle loss. It causes quantum particles to behave as classical ones, whose statistics cannot mimic quantum coherence and therefore we observe a transition from the quantum to the classical domain.

V. SSH AND GENERALISED SSH SPIN CHAIN

As we saw in the main text, a general chiral XY spin chain is represented by the Hamiltonian

$$H_{XY} = \sum_{n=1}^{S} \tfrac{J_n}{2} \left(\sigma_n^x \sigma_{n+1}^x + \sigma_n^y \sigma_{n+1}^y\right) = \sum_{n=1}^{S} J_n \left(\sigma_n^+ \sigma_{n+1}^- + \sigma_n^- \sigma_{n+1}^+\right). \tag{S20}$$

In the single excitation subspace this Hamiltonian has matrix elements

$$\mathbf{H} \equiv [\mathbf{H}_{XY}]^{\text{Spin}} = \begin{pmatrix} 0 & J_1 & 0 & \dots & 0 \\ J_1 & 0 & J_2 & \dots & 0 \\ 0 & J_2 & 0 & \dots & 0 \\ . & . & . & \dots & . \\ . & . & . & \dots & . \\ . & . & . & \dots & J_S \\ 0 & 0 & 0 & J_S & 0 \end{pmatrix}, \tag{S21}$$

where $[\mathbf{H}_{XY}]^{\text{Spin}}_{mn} = \langle m| H_{XY} |n\rangle$, $|m\rangle = \sigma_m^+ |\downarrow\downarrow\downarrow \dots\rangle$, and σ_n^x, σ_n^y and $\sigma_n^\pm = (1/2)(\sigma_n^x \pm i\sigma_n^y)$ are Pauli operators acting on the nth spin.

A. SSH model

Couplings of $J_n = 2J(1 + \delta(-1)^n)$ correspond to the SSH model. Figure S3 shows the zero-energy state close to the topological transition. It is a superposition of two edge states which are of the form (e.g. the left edge) $\sum_{n=1}^{(S+1)/2} (-1)^n e^{-2n/\xi} \sigma_{2n}^+ |\downarrow\downarrow\downarrow \dots\rangle$, where $\xi = 2/\ln\left(\frac{1+\delta}{1-\delta}\right)$ is the localisation length [38]. In much the same way as the topological edge states of the generalised SSH model discussed in the main text, here we see that the conventional SSH model can also present weakly localised edge states that are nonetheless topological, see Fig. S3.

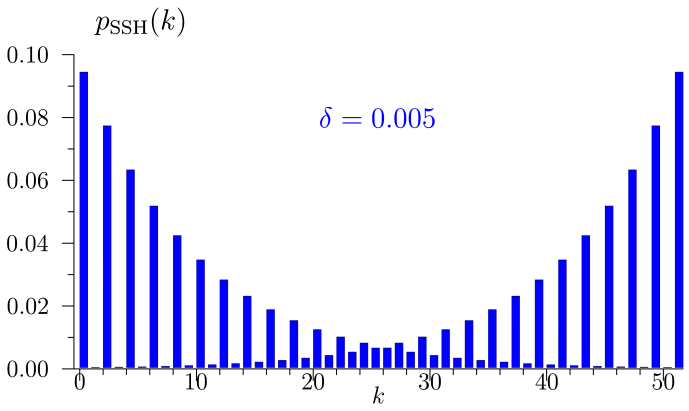

FIG. S3: Probability densities of the zero-energy edge state of the SSH model for a chain of length $S + 1 = 52$. Here $\delta = 0.005$.

B. Generalised SSH model

The photonic system simulates a spin chain with couplings $J_n = \frac{\hbar}{2}\sqrt{n(S+1-n)}$. This model belongs to a non-trivial class in the periodic table of topological insulators, as defined by the Altland–Zirnbauer symmetry classes [31]. A system is categorised according to the properties of its time-reversal operator $\mathbf{T} = \mathbf{U}_T \mathcal{K}$, charge-conjugation operator $\mathbf{C} = \mathbf{U}_C \mathcal{K}$, and chiral-symmetry operator $\mathbf{\Gamma} = \mathbf{TC}$, where $\mathbf{U}_{T(C)}$ is a unitary operator and $\mathcal{K}$ is complex conjugation. If there exists a $\mathbf{T}$ ($\mathbf{C}$ or $\mathbf{\Gamma}$) that commutes (anti-commutes) with $\mathbf{H}$ than the system is said to possess the respective symmetry and is classified according to the square of that operator. $\mathbf{H}$ is real-valued and thus its

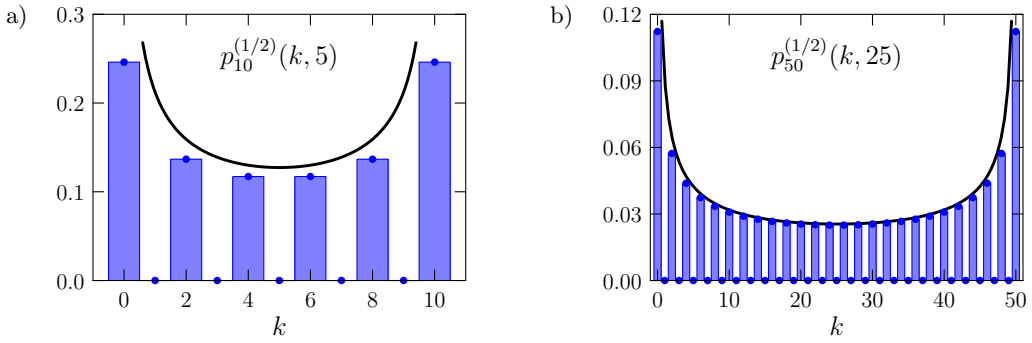

FIG. S4: Photon-number statistics $p_S^{(1/2)}(k,\frac{S}{2})$ for (a) $S=10$, (b) $S=50$ photons. The solid curve is an asymptotic envelope described in the text.

time-reversal symmetry operator is simply $\mathbf{T}=\mathbf{1}\mathcal{K}$. Due to the absence of couplings beyond nearest-neighbour the chiral symmetry operator is given by $\mathbf{\Gamma}_{ij}=(-\delta_{ij})^2$, and finally $\mathbf{C}=\mathbf{TT}$. Our system possesses all three symmetries with $(\mathbf{T}^2,\mathbf{C}^2,\mathbf{\Gamma}^2)=(1,1,1)$. Thus it belongs to the BDI (chiral orthogonal) class of topological insulators which in one-dimension is characterised by a $\mathbb{Z}$ topological invariant. The zero-energy eigenmode for a chain of length $S+1=50$ (discussed more in section VI) is shown in Figure 2 of the main text.

VI. EDGE STATES

Let us find the eigenstates of H_{BS}, Eq. 1 and see if there are any edge states among them. To this end we employ the following transformation

$$\mathcal{O}^\dagger a\,\mathcal{O}=\tfrac{a-b}{\sqrt{2}},\ \mathcal{O}^\dagger b\,\mathcal{O}=\tfrac{a+b}{\sqrt{2}} \tag{S22}$$

where $\mathcal{O}=U_{BS}^{(1/2,\pi)}$, and diagonalize this Hamiltonian in the basis of Fock states

$$H_{BS}^{\rm diag}=\mathcal{O}^\dagger\,H_{BS}\,\mathcal{O}=\frac{1}{2}\left(a^\dagger a-b^\dagger b\right). \tag{S23}$$

Thus, the eigenstates of $H_{BS}^{\rm diag}$ are two-mode Fock states

$$H_{BS}^{\rm diag}\,|l,S-l\rangle\ =(l-S/2)\,|l,S-l\rangle\,, \tag{S24}$$
$$\mathcal{O}^\dagger H_{BS}\mathcal{O}\,|l,S-l\rangle\ =(l-S/2)\,|l,S-l\rangle\,, \tag{S25}$$
$$H_{BS}\,(\mathcal{O}\,|l,S-l\rangle)\ =(l-S/2)\ (\mathcal{O}\,|l,S-l\rangle)\,. \tag{S26}$$

Thus, $|\Psi_l^{(S,1/2,\pi)}\rangle\equiv\mathcal{O}\,|l,S-l\rangle$ are eigenstates of H_{BS} with eigenvalues $l-S/2$.
Please note that for $l=\frac{S}{2}$, the eigenstate $\left|\Psi_{S/2}^{(S,1/2,\pi)}\right\rangle$ is a zero-energy mode

$$H_{BS}\left|\Psi_{S/2}^{(S,1/2,\pi)}\right\rangle=0. \tag{S27}$$

We examine its photon-number statistics $p_S^{(1/2)}(k,\frac{S}{2})=\left|\phi_k^{(1/2)}(0,S)\right|^2$ in Fig. S4. For large S, the function $\frac{4}{\pi S\sqrt{1-(2k/(S-1))^2}}$ provides an asymptotic envelope to $p_S^{(1/2)}(k,\frac{S}{2})$, shown as a solid curve in Fig. S4.

VII. EXPERIMENTAL METHODS

In the experiment, Fig. 1(b), a light pulse from a titanium-sapphire laser at 775 nm (FWHM of 2 nm; repetition rate 75 kHz) pumped two collinear type-II phase-matched 8 mm-long SPDC waveguides written in a periodically poled

KTP (PP-KTP) crystal. They generated independent two-mode squeezed vacuum states $|\Psi\rangle = \sum_{n=0}^{\infty} \lambda_n \, |n,n\rangle_{1,2}$, where 1 and 2 denote two output modes, named the signal and idler, $\lambda_n = \frac{\tanh^n g}{\cosh g}$ is a probability of creation of a pair of n photons and g is the parametric gain. The average photon number in each mode equals $\langle \hat{n} \rangle = \sinh^2 g$. We achieved an average photon number of $\langle \hat{n} \rangle \approx 0.2$, which was sufficient to ensure the emission of multi-photon pairs. A polarizing beam splitter split the squeezed vacua into four spatial modes a–d. They were filtered by bandpass filters with 3 nm FWHM angle-tuned to the central wavelength (1554 nm – signal modes a and b, 1546 nm – idler modes c and d) in order to reduce the background [49]. The modes c and d were used for heralding and conditional creation of Fock states in modes a and b. They interfered in a variable ratio phase-matched fiber coupler, which allows one to set the ratio between 0 and 100% with an error of ±1.5%. We employed transition-edge sensors running at 70 mK which allow for photon-number resolved measurements in all modes [50].

Measurements for each setting of the splitting ratio were taken over 400 seconds, giving 10^9 samples for $r \in [0, 1]$. The measurement errors for each mode were estimated to $\Delta p = \frac{1}{\sqrt{N}}$, where N is the number of events for a given number of photons in modes a and b.

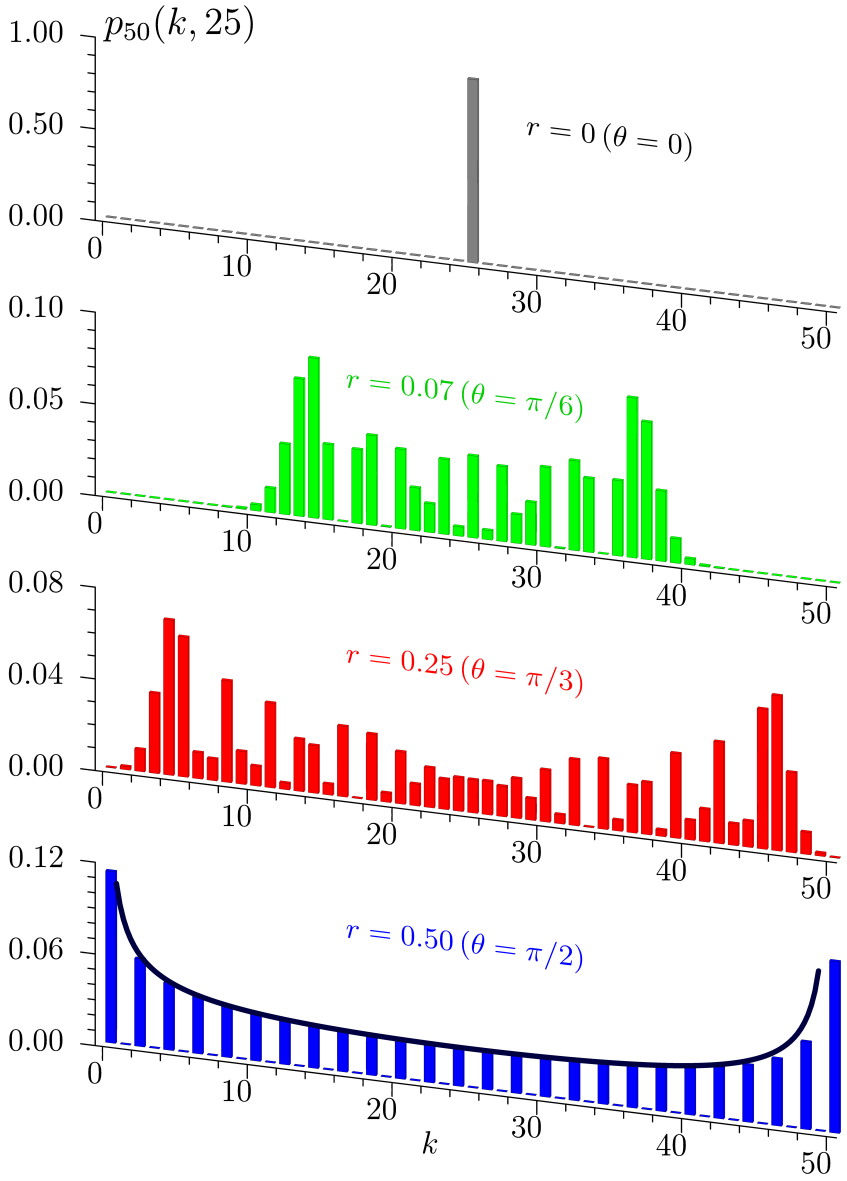
$p_{50}(k, 25)$
1.00
0.50
0.00
$r = 0\ (\theta = 0)$
0
10
20
30
40
50
0.10
0.05
0.00
$r = 0.07\ (\theta = \pi/6)$
0.08
0.04
0.00
$r = 0.25\ (\theta = \pi/3)$
0.12
0.06
0.00
$r = 0.50\ (\theta = \pi/2)$
k